CMS Physics Analysis Summary

Contact: cms-pag-conveners-top@cern.ch 2024/08/05

Search for lepton flavour violation in top quark interactions with an up-type quark, a muon, and a τ lepton

The CMS Collaboration

Abstract

We present a search for charged-lepton flavour violation (CLFV) in the top quark (t) sector using 138 fb^{-1} of proton-proton collision data collected with the CMS experiment at a centre-of-mass energy of 13 TeV. The analysis focuses on events containing a single muon (μ) and a hadronically decaying τ lepton. Machine learning multiclass classification techniques are used to distinguish signal from standard model background events. The CLFV signal consists of the production of a single top quark via a CLFV interaction or top quark pair production followed by a CLFV decay. The results of this search are consistent with the standard model expectations. The upper limits at 95% confidence level on the branching fraction $\mathcal{B}$ for CLFV top quark decays to an up (u) or a charm (c) quark, a muon and a τ lepton are $\mathcal{B}(\text{t} \to \mu\tau\text{u}) < 0.04$, 0.078, and 0.118×10^{-6}, and $\mathcal{B}(\text{t} \to \mu\tau\text{c}) < 0.81$, 1.71, and 2.05×10^{-6} for scalar, vector, and tensor-like operators, respectively.

1 Introduction

The standard model (SM) of particle physics is very successful in describing the properties of all elementary particles and their interactions with a small number of free parameters, but it is known to be incomplete. Extensions of the SM aim to describe several observed phenomena such as the nature of dark matter [1–4] or the baryon asymmetry of the universe [5].

The observation of neutrino oscillations [6] confirms a nonzero neutrino mass and neutral-lepton flavour violation. The existence of neutrino mass terms implies charged-lepton flavour violation (CLFV) in the SM at the loop level. An example is the CLFV branching fraction $\mathcal{B}$ of a muon decay into an electron and a photon, which is of the order of 10^{-55} in the SM, whereas extensions of the SM predict branching fractions as high as 10^{-4} [7]. The observation of CLFV would be a decisive signature of new physics beyond the SM.

Recent combinations of B meson decay rates report a tension between the SM predictions and the measured values for ratios of B decays into D and D^* mesons [8]. This has sparked interest in models that aim to explain these deviations, and at the same time introduce a new source of lepton flavour violation (LFV) effects. For example, leptoquark models developed to explain the anomalies in the b quark sector could generate a four-fermion interaction that would allow the $t \to c\ell_i\ell_j$ decay at the tree level [9], where ℓ denotes a charged lepton and the indices i and j denote the generation. Recently, the LHCb Collaboration reported a combined deviation of 1.9 standard deviations from the SM values for the ratios of B meson branching fractions into D and D^* mesons [10], renewing interest in the search for LFV.

The ATLAS Collaboration has performed a search for CLFV in $\mu\tau qt$ interactions using data corresponding to 140 fb^{-1} at a centre-of-mass energy $\sqrt{s} = 13$ TeV [11]. Events are selected with two muons, one hadronically decaying τ lepton (τ_h), and at least one jet identified to originate from the fragmentation of a b quark (b jet), resulting in an upper limit at 95% confidence level (CL) of $\mathcal{B}(t \to \mu\tau q) < 8.7 \times 10^{-7}$, where q can be a u or c quark. The CMS Collaboration has performed searches for CLFV involving $e\mu tq$ interactions in dilepton and trilepton final states [12, 13]. The upper limits at 95% CL on the corresponding branching fractions range from 10^{-6} to 10^{-8}.

A search for CLFV involving interactions with top quarks is presented in this note. The analysis uses data collected with the CMS detector at $\sqrt{s} = 13$ TeV, corresponding to an integrated luminosity of 138 fb^{-1}. We consider final states with a muon and a τ_h with opposite charge, and a jet from a u or c quark. The analysis focuses on CLFV single top quark (ST CLFV) production and top quark pair production ($t\bar{t}$) with a subsequent CLFV decay (TT CLFV), as illustrated in Fig. 1. Signal events are modelled using an effective field theory (EFT) framework with dimension-6 operators $O^{(6)}$ and the corresponding Wilson coefficients $C_a^{(6)}$, where the La-

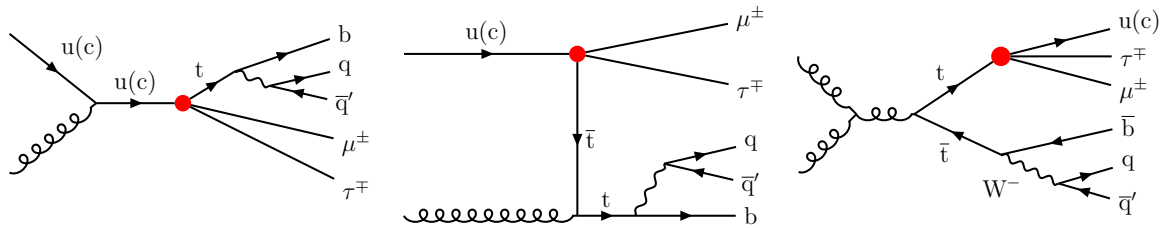

Figure 1: Example Feynman diagrams at leading order for the CLFV single production of a top quark (left and centre) and top quark pair production followed by a CLFV decay (right)

Table 1: The EFT operators considered in this analysis and their definition. The ε is a fully antisymmetric two-dimensional matrix, γ^μ are the Dirac matrices, and $\sigma^{\mu\nu} = \frac{i}{2}[\gamma^\mu, \gamma^\nu]$. Left-handed doublets of leptons and quarks are denoted by ℓ_i and q_k, respectively, where the indices i and k denote the lepton and quark flavours. Right-handed lepton and quark singlets are denoted by e_i and u_k, respectively. The operator $O^1_{\ell q}$ represents the left-handed fermion interaction $O_{\ell q}$.

Structure	Operator	Definition	Wilson coefficient
Scalar	$O^{1(ijkl)}_{\ell equ}$	$(\overline{\ell}_i e_j)\varepsilon(\overline{q}_k u_l)$	$C_{\ell equ1}$
Vector	$O^{1(ijkl)}_{\ell q} = O_{\ell q}$	$(\overline{\ell}_i \gamma^\mu \ell_j)(\overline{q}_k \gamma^\mu q_l)$	$C_{\ell q}$
	$O^{(ijkl)}_{\ell u}$	$(\overline{\ell}_i \gamma^\mu \ell_j)(\overline{u}_k \gamma^\mu u_l)$	$C_{\ell u}$
	$O^{(ijkl)}_{eq}$	$(\overline{e}_i \gamma^\mu e_j)(\overline{q}_k \gamma^\mu q_l)$	C_{eq}
	$O^{(ijkl)}_{eu}$	$(\overline{e}_i \gamma^\mu e_j)(\overline{u}_k \gamma^\mu u_l)$	C_{eu}
Tensor	$O^{3(ijkl)}_{\ell equ}$	$(\overline{\ell}_i \sigma^{\mu\nu} \ell_j)\varepsilon(\overline{q}_k \sigma_{\mu\nu} u_l)$	$C_{\ell equ3}$

grangian has the form

$$\mathcal{L}_{\text{eff}} = \mathcal{L}_{\text{SM}} + \frac{1}{\Lambda^2}\sum_a C_a^{(6)} O_a^{(6)} + \mathcal{O}\left(\frac{1}{\Lambda^4}\right).$$

The sum runs over all operators introducing CLFV effects and the new physics scale Λ is set to 1 TeV. Terms of order $1/\Lambda^4$ and higher are neglected. Table 1 summarizes the EFT operators considered in this analysis and their grouping according to the Lorentz structure.

This note is organized as follows. We start with a brief overview of the CMS detector in Section 2. A detailed description of the signal and background modelling is presented in Section 3. In Section 4, we describe the physics objects and the selection requirements, followed by improvements of the background modelling in Section 5. The reconstruction of the top quarks and W bosons, as well as the signal discrimination are explained in Section 6. Systematic uncertainties which contribute to the analysis are listed in Section 7. The results of the search are presented in Section 8 and we conclude with a summary in Section 9.

2 The CMS detector

The central feature of the CMS apparatus is a superconducting solenoid of 6 m internal diameter, providing a magnetic field of 3.8 T. Within the solenoid volume are a silicon pixel and strip tracker, a lead tungstate crystal electromagnetic calorimeter (ECAL), a brass and scintillator hadron calorimeter (HCAL), each composed of a barrel and two endcap sections. Forward calorimeters extend the pseudorapidity coverage provided by the barrel and endcap detectors.

Events of interest are selected using a two-tiered trigger system. The first level, composed of custom hardware processors, uses information from the calorimeters and muon detectors to select events at a rate of around 100 kHz within a fixed latency of 4 μs [14]. The second level, known as the high-level trigger (HLT), consists of a farm of processors running a version of the full event reconstruction software optimized for fast processing, and reduces the event rate to around 1 kHz before data storage [15]. A more detailed description of the CMS detector, together with a definition of the coordinate system used and the relevant kinematic variables, can be found in Ref. [16].

3 Data and simulated samples

Data events were collected with the CMS detector in proton-proton (pp) collisions in the years 2016 to 2018 at $\sqrt{s} = 13\,\text{TeV}$, corresponding to an integrated luminosity of $138\,\text{fb}^{-1}$. The data analysed in this search were recorded by triggers requiring the presence of a single muon. We use HLT paths with isolated muons [17], where the muon transverse momentum (p_T) thresholds vary between 24–27 GeV, depending on the data-taking period.

Signal LFV events are generated at leading order (LO) accuracy with MADGRAPH5_aMC@NLO 2.6.5 [18], separately for single top quark and $\text{t}\bar{\text{t}}$ production using the SMEFTFR model [19]. The ST CLFV cross sections are calculated at LO with MADGRAPH5_aMC@NLO, while the TT CLFV signal cross sections are calculated based on the results from Refs. [20, 21], multiplied by the SM $\text{t}\bar{\text{t}}$ cross section of 833.9 pb as obtained from the TOP++ program at next-to-next-to-LO (NNLO) in perturbative quantum chromodynamics (QCD) including soft-gluon resummation at next-to-next-to-leading-logarithmic (NNLL) order [22]. We use MADGRAPH5_aMC@NLO to assign weights to simulated signal events such that the kinematics and normalization of the signal samples resemble the predictions from SMEFTSIM [23] as done in Ref. [13]. The event weight is computed by comparing the matrix element amplitudes of SMEFTFR and SMEFTSIM for each event. The method is validated using signal samples generated with SMEFTSIM. Table 2 summarizes the predicted cross sections for each channel considered with the Wilson coefficients set to $C_a/\Lambda^2 = 1\,\text{TeV}^{-2}$.

The top quark p_T spectrum in $\text{t}\bar{\text{t}}$ production simulated at LO and next-to-LO (NLO) differs from higher-order theoretical predictions [24–26]. Therefore, the distribution in the top quark p_T in the TT CLFV events is corrected sequentially from LO to NLO and to the NNLO QCD+NLO electroweak prediction [27, 28] utilising simulated SM $\text{t}\bar{\text{t}}$ samples and theory predictions [27, 28], respectively.

Background processes are divided into three groups: $\text{t}\bar{\text{t}}$ pair production, single top quark production, and the others. These are referred to as "$\text{t}\bar{\text{t}}$", "single t", and "other", respectively. The largest background process is SM $\text{t}\bar{\text{t}}$ pair production in the lepton+jets and dileptonic decay channels. It is simulated at NLO precision using POWHEG v2 [29–31]. The p_T spectrum in the SM $\text{t}\bar{\text{t}}$ sample is corrected to match the NNLO predictions, similar to the TT CLFV signal samples. The single t background consists of t-channel and s-channel processes, and W-boson associated production (tW). These are simulated at NLO accuracy using POWHEG v2, MAD-

Table 2: Predicted cross sections for CLFV signal processes. Operators with different Lorentz structures are considered with $C_a/\Lambda^2 = 1\,\text{TeV}^{-2}$. The results for ST CLFV are at LO accuracy and the ones for TT CLFV are at NNLO+NNLL accuracy for the $\text{t}\bar{\text{t}}$ production with LO accuracy for the CLFV decay.

Process	Lorentz structure	Cross sections (fb)
ST CLFV $\text{tu}\mu\tau$	Scalar	59.14
	Vector	276.1
	Tensor	1272
ST CLFV $\text{tc}\mu\tau$	Scalar	3.74
	Vector	19.51
	Tensor	96.18
TT CLFV $\text{tq}\mu\tau$	Scalar	2.69
	Vector	21.5
	Tensor	129.0

GRAPH5_aMC@NLO, and POWHEG v2 [32], respectively. The predicted NLO cross sections are 134 and 80 pb for t-channel top quark and antiquark production, respectively, and 6.8 pb for s-channel production [33, 34]. The tW cross section is 79.3 pb, calculated at approximate NNLO accuracy [35, 36]. Other smaller SM background contributions arise from $\mathrm{t\bar{t}}$ production in fully hadronic decays, $\mathrm{t\bar{t}}$ production in association with a vector boson ($\mathrm{t\bar{t}Z}$ and $\mathrm{t\bar{t}W}$) or a Higgs boson ($\mathrm{t\bar{t}H}$), simulated with MADGRAPH5_aMC@NLO and POWHEG v2 at NLO accuracy, respectively, Drell–Yan and W boson production, simulated with MADGRAPH5_aMC@NLO at LO with up to 4 additional jets using MLM matching [37], and diboson (WW, WZ, and ZZ) processes generated with PYTHIA 8.240 [38] at LO accuracy. The parton distribution function (PDF) set used for the event generation is NNPDF 3.1 [39], while PYTHIA with the CP5 tune [40] is used to simulate initial- and final-state radiation, the parton shower, and the hadronization process. All simulated samples are interfaced to GEANT4 [41] for a detailed simulation of the CMS detector response.

4 Object reconstruction and event selection

The particle-flow (PF) algorithm [42] aims to reconstruct and identify each individual particle in an event, with an optimized combination of information from the various elements of the CMS detector including charged particle tracks from the tracking detector, energy deposits in the HCAL and ECAL, and reconstructed tracks from the muon chambers. Particles in each event are reconstructed and identified as either electrons, muons, photons, charged hadrons, or neutral hadrons. The primary vertex is taken to be the vertex corresponding to the hardest scattering in the event, evaluated using tracking information alone, as described in Section 9.4.1 of Ref. [43]. The number of reconstructed vertices in the simulated samples is corrected assuming an inelastic pp collision cross section of 69.2 mb.

Muons are identified as tracks in the central tracker consistent with either a track or several hits in the muon system, and associated with calorimeter deposits compatible with the muon hypothesis. The energy of muons is obtained from the curvature of the corresponding track. Muons are required to have a p_{T} of at least 50 GeV and a $|\eta|$ less than 2.4, where η denotes the pseudorapidity. Moreover, muons need to be isolated and pass the "tight" identification criteria, which corresponds to a 96% efficiency [44]. The muons passing "loose" isolation and identification criteria are used to veto events with additional muons.

Electrons are identified as a primary charged particle track and potentially multiple ECAL energy clusters corresponding to the extrapolation of this track to the ECAL and to possible bremsstrahlung photons emitted along the way. The electron momentum is estimated by combining the energy measurement in the ECAL with the momentum measurement in the tracker. Electrons are introduced to reject events with additional leptons, and only electrons passing the "veto" cut-based identification [45] with $p_{\mathrm{T}} > 15$ GeV and $|\eta| < 2.4$ are considered.

Charged hadrons are identified as charged particle tracks that are neither identified as electrons nor muons. Finally, neutral hadrons are identified as HCAL energy clusters not linked to any charged hadron trajectory, or as a combined ECAL and HCAL energy excess with respect to the expected charged hadron energy deposit. The energy of charged hadrons is determined from a combination of their momentum measured in the tracker and the matching ECAL and HCAL energy deposits, corrected for the response function of the calorimeters to hadronic showers. The energy of neutral hadrons is obtained from the corresponding corrected ECAL and HCAL energy deposits.

The PF candidates are clustered into jets using the anti-k_{T} clustering algorithm [46] with a dis-

tance parameter of 0.4, implemented in the FASTJET package [47, 48]. The jet momentum is determined as the vectorial sum of all particle momenta in the jet, and is found from simulation to be, on average, within 5–10% of the true momentum over the entire p_T spectrum and detector acceptance. Additional pp interactions within the same or nearby bunch crossings (pileup) can contribute additional tracks and calorimetric energy depositions to the jet momentum. To mitigate this effect, tracks identified as originating from pileup vertices are discarded and a correction is applied for the remaining contributions. Jet energy corrections are derived from simulation studies so that the average measured energy of reconstructed jets becomes identical to that of particle-level jets. In situ measurements of the momentum balance in dijet, photon+jet, Z+jet, and multijet events are used to determine any residual differences between the jet energy scale (JES) in data and in simulation, and appropriate corrections are made [49]. The jet energy resolution (JER) amounts typically to 15–20% at 30 GeV, 10% at 100 GeV, and 5% at 1 TeV [49]. Heavy-flavor jets are identified based on the DEEPJET algorithm [50–52] at a working point defined by a light-quark or gluon jet misidentification rate of 1%, resulting in a b jet identification efficiency of 75%. Only jets with $p_T > 40$ GeV and $|\eta| < 2.4$ are considered, and the b-tagged jet is selected using the DEEPJET algorithm.

Hadronic τ decays (τ_h) are reconstructed from jets, using the hadrons-plus-strips algorithm [53], which combines one or three tracks with energy deposits in the calorimeters, to identify the τ_h lepton decay modes. Neutral pions are reconstructed as strips with dynamic size in η-ϕ, with ϕ denoting the azimuthal angle, from reconstructed electrons and photons [45]. The strip size varies as a function of the p_T of the electron or photon candidate. To distinguish genuine τ_h decays from jets originating from the hadronization of quarks or gluons, and from electrons or muons, the DEEPTAU algorithm is used [54]. Information from all individual reconstructed particles near the τ_h axis is combined with properties of the τ_h candidate and the event. The rate of a jet to be misidentified as τ_h by the DEEPTAU algorithm depends on the p_T and quark flavour of the jet. In simulated events from W boson production in association with jets, it has been estimated to be 0.43% for a genuine τ_h identification efficiency of 70%. The misidentification rates for electrons and muons are 2.60 and 0.03% for genuine τ_h identification efficiencies of 80 and >99%, respectively. The τ_h energy scale corrections are derived from a binned maximum likelihood fit of the distributions of observables sensitive to the energy shift [53, 54]. The τ_h are required to pass kinematic requirements of $p_T > 40$ GeV and $|\eta| < 2.3$. Candidates are selected using the "very tight" criteria to discriminate against quark and gluon jets, and the "tight" and "very loose" criteria against muons and electrons, respectively. The chosen identification working points have τ_h efficiencies of about 50, 98, and 98.8% with misidentification probabilities of about 0.4, 2 and 0.02% for the discrimination against jets, electrons, and muons, respectively [54].

The missing transverse momentum vector $\vec{p}_T^{\,miss}$ is computed as the negative vector p_T sum of all the PF candidates in an event, and its magnitude is denoted as p_T^{miss} [55]. The $\vec{p}_T^{\,miss}$ is modified to account for corrections to the energy scale of the reconstructed jets in the event.

The event selection is designed to isolate final state particles characteristic of CLFV signal processes in both single top and top quark pair production. Events are selected via a sequence of requirements on selected physics objects. Events must have exactly one isolated muon with no additional muons or electrons. Furthermore, events with exactly one τ_h candidate are selected, separated by $\Delta R > 0.4$ from the muon. The angular distance ΔR is defined as $\Delta R = \sqrt{\Delta\eta^2 + \Delta\phi^2}$, where $\Delta\eta$ and $\Delta\phi$ are the differences in pseudorapidity and azimuthal angle between the τ_h and muon candidates, respectively. Only events containing an oppositely charged muon-τ_h pair are considered. We remove jets with $\Delta R < 0.4$ from the selected muon and τ_h candidates. Events must contain at least 3 jets, where one jet has to be b tagged.

The lepton identification efficiencies for the muon and τ_h candidates used in this analysis are measured using the "tag-and-probe" technique [56]. Efficiency differences between data and simulation are corrected for by applying scale factors to the simulation.

5 Background estimation: Jets misidentified as τ_h

Despite the discrimination power of the DEEPTAU algorithm with a τ_h misidentification probability of less than 1% for light-flavour and gluon jets, a nonnegligible background contribution remains from events with misidentified τ_h candidates. Most of these are $t\bar{t}$ events in the lepton+jets decay channel, where the correctly identified muon originates from the top quark decay chain $t \to Wb \to \mu\nu b$. Other events with a misidentified τ_h candidate originate from W+jet and single t production. Because of the much smaller muon misidentification rate, events with a misidentified muon and a genuine τ_h candidate are negligible compared to events with a misidentified τ_h candidate. The rate of misidentified τ_h candidates is not well modelled by simulation, therefore a data-driven approach is used to calculate the contribution of events with a misidentified τ_h candidate in this analysis.

The ABCD method, as introduced in Ref. [57], uses additional event categories to calculate scaling factors for simulated events with a misidentified τ_h candidate. The signal region D contains events that pass all selections of Section 4, with muon and τ_h candidates having opposite charges. An inversion of the charge requirement defines control region B, where the muon and τ_h candidates have the same charge. Additional control regions are constructed by requiring events to have a τ_h candidate passing the "loose", but failing the "very tight" requirement of the τ_h discrimination against jets. These events enter region A if the muon and τ_h candidates have the same charge, and region C if they have opposite charges. The same requirements on the jet and b jet multiplicities are applied to all regions. The number of events with a misidentified τ_h candidate in region D, $N^{\mathrm{D}}_{\text{mis-ID}}$, is calculated from data in regions A, B, and C,

$$N^{\mathrm{D}}_{\text{mis-ID}} = N^{\mathrm{C}} \frac{N^{\mathrm{B}}}{N^{\mathrm{A}}}. \tag{1}$$

In each region i, the number of events N^i entering Eq. (1) is the number of observed events in data N^i_{obs} corrected for the number of events with a genuine τ_h lepton N^i_{genuine},

$$N^i = N^i_{\text{obs}} - N^i_{\text{genuine}}, \tag{2}$$

where N^i_{genuine} is determined using generator-level information in simulated events. The ABCD method corrects the normalization of simulated background processes with misidentified τ_h candidates in the signal region D under the assumption that the ratio between the number of jets misidentified as τ_h passing the "very tight" and "loose" selection criteria is the same for same-sign and opposite-sign events. The scale factor applied to simulated events is calculated as $N^D_{\text{mis-ID}}/(N^D_{\text{tot. bkg.}} - N^D_{\text{genuine}})$, where $N^D_{\text{tot. bkg.}}$ is the number of all simulated background events in region D. This scale factor is calculated and applied separately for each data-taking period and τ_h decay mode.

We show distributions of important event properties in Fig. 2, after the event selection of Section 4. Distributions obtained from data are compared to distributions from the sum of all background processes, including the scale factors from the ABCD method. The signal processes are normalized to the total number of events observed in data for visibility.

The total number of expected events for CLFV signal and background processes, where the

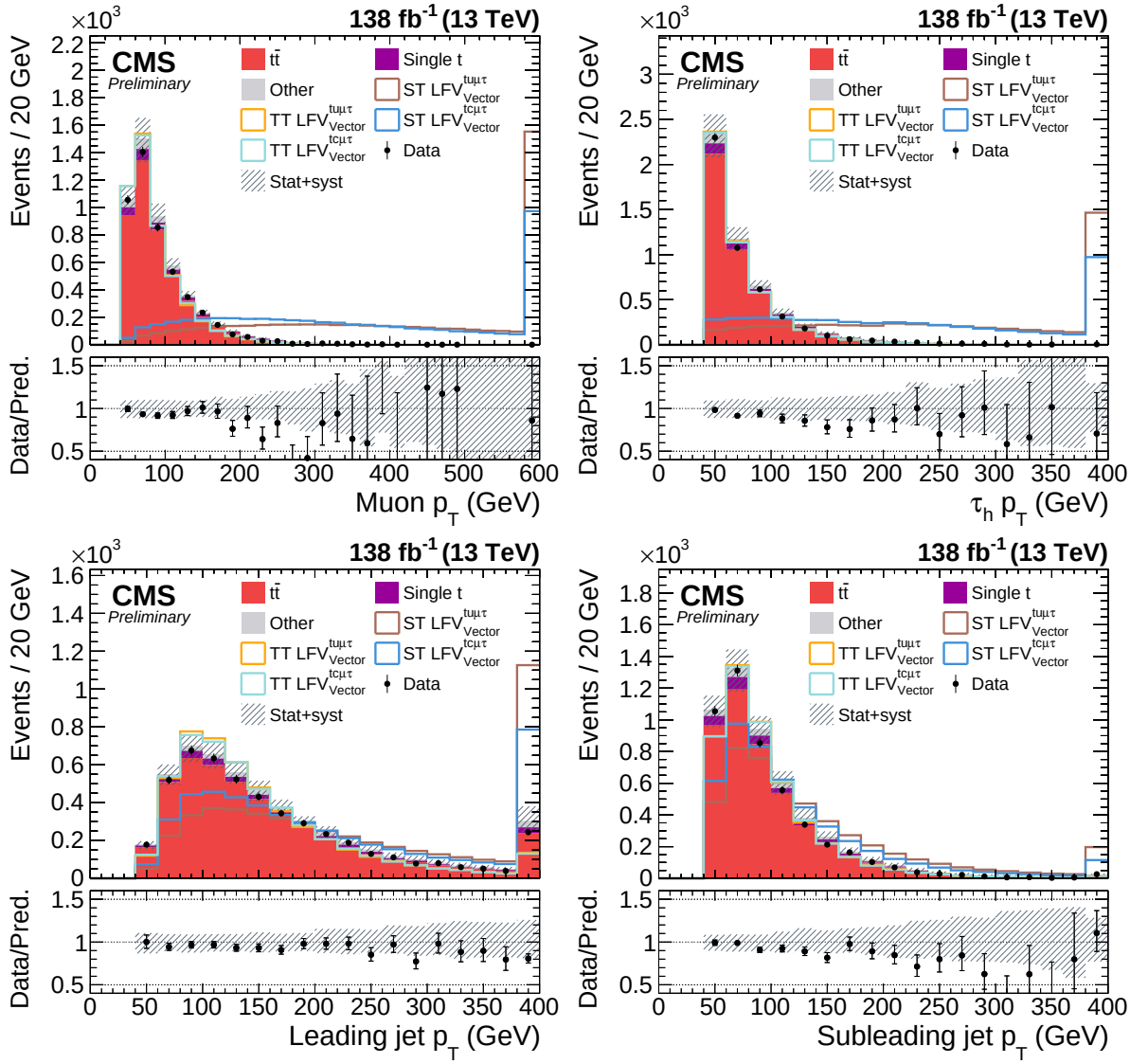

Figure 2: Distributions in p_T of the muon (top left), τ_h (top right), p_T-leading jet (bottom left), and p_T-trailing jet (bottom right) after all selection steps. The solid lines show the signal distributions, individually for each type of operator and interaction. The signals are normalized to the total number of events in data for visibility. The last bin in each histogram contains the overflow. The shaded band displays the total uncertainty in the predicted background, consisting of statistical and systematic uncertainties. The panels below the distributions show the ratio of data to the background prediction.

Table 3: Estimated event yields including the background corrections from the ABCD method discussed in Sec 5. The numbers shown correspond to observed events before the maximum-likelihood fit described in Section 8. Only statistical uncertainties are shown, related to the size of the data sets.

Process	Event yield
ST CLFV tu$\mu\tau$ Scalar	535 $\pm$ 1
ST CLFV tu$\mu\tau$ Vector	2327 $\pm$ 3
ST CLFV tu$\mu\tau$ Tensor	9909 $\pm$ 13
ST CLFV tc$\mu\tau$ Scalar	32 $\pm <$ 1
ST CLFV tc$\mu\tau$ Vector	129 $\pm <$ 1
ST CLFV tc$\mu\tau$ Tensor	701 $\pm$ 1
TT CLFV tu$\mu\tau$ Scalar	1.1 $\pm <$ 0.1
TT CLFV tu$\mu\tau$ Vector	8.2 $\pm <$ 0.1
TT CLFV tu$\mu\tau$ Tensor	48 $\pm <$ 1
TT CLFV tc$\mu\tau$ Scalar	1.1 $\pm <$ 0.1
TT CLFV tc$\mu\tau$ Vector	7.9 $\pm <$ 0.1
TT CLFV tc$\mu\tau$ Tensor	45 $\pm <$ 1
$\mathrm{t\bar{t}}$	4573 $\pm$ 13
Single Top	306 $\pm$ 9
Other	258 $\pm$ 5
Total $\pm$ (stat)	5136 $\pm$ 17
Data	4810
Data / Background prediction	0.94 $\pm$ 0.01

background yields include τ_h misidentification scale factors from the ABCD method, are presented in Table 3 and compared to data.

6 Discrimination of signal and background

6.1 Reconstruction of top quark and W boson

In both ST CLFV and TT CLFV signal events, a top quark is produced that decays hadronically through the decay chain $\mathrm{t} \to \mathrm{bW} \to \mathrm{bq\bar{q}'}$. Background events mostly originate from $\mathrm{t\bar{t}}$ production in the dileptonic decay channel. To benefit from this difference, the hadronic top quark decay is reconstructed using a χ^2 method. The χ^2 variable is constructed as

$$\chi^2 = \left(\frac{m_\mathrm{t} - m_\mathrm{bjj'}}{\sigma_\mathrm{t}}\right)^2 + \left(\frac{m_\mathrm{W} - m_\mathrm{jj'}}{\sigma_\mathrm{W}}\right)^2, \tag{3}$$

with the expected mass values $m_\mathrm{t} = 173.95\,\mathrm{GeV}$ and $m_\mathrm{W} = 84.2\,\mathrm{GeV}$, and resolutions $\sigma_\mathrm{t} = 17.07\,\mathrm{GeV}$ and $\sigma_\mathrm{W} = 9.91\,\mathrm{GeV}$. The mass and resolution values are computed in simulated $\mathrm{t\bar{t}}$ events from detector-level jets matched to generator-level jets from the top quark and W boson decays. The χ^2 is calculated for all possible combinations of non-b-tagged jets in an event. The reconstructed W boson candidate is formed by two jets with mass $m_\mathrm{jj'}$ and the selected b-tagged jet is assigned to the reconstructed top quark candidate with mass $m_\mathrm{bjj'}$. For each event, the reconstruction hypothesis is chosen that results in the smallest value of χ^2.

The results of the reconstruction are presented in Fig. 3 for data, simulated signal and background events. The scale factors from the ABCD method are applied to the background simulation. Distributions in signal events show more pronounced peaks around m_t and m_W in

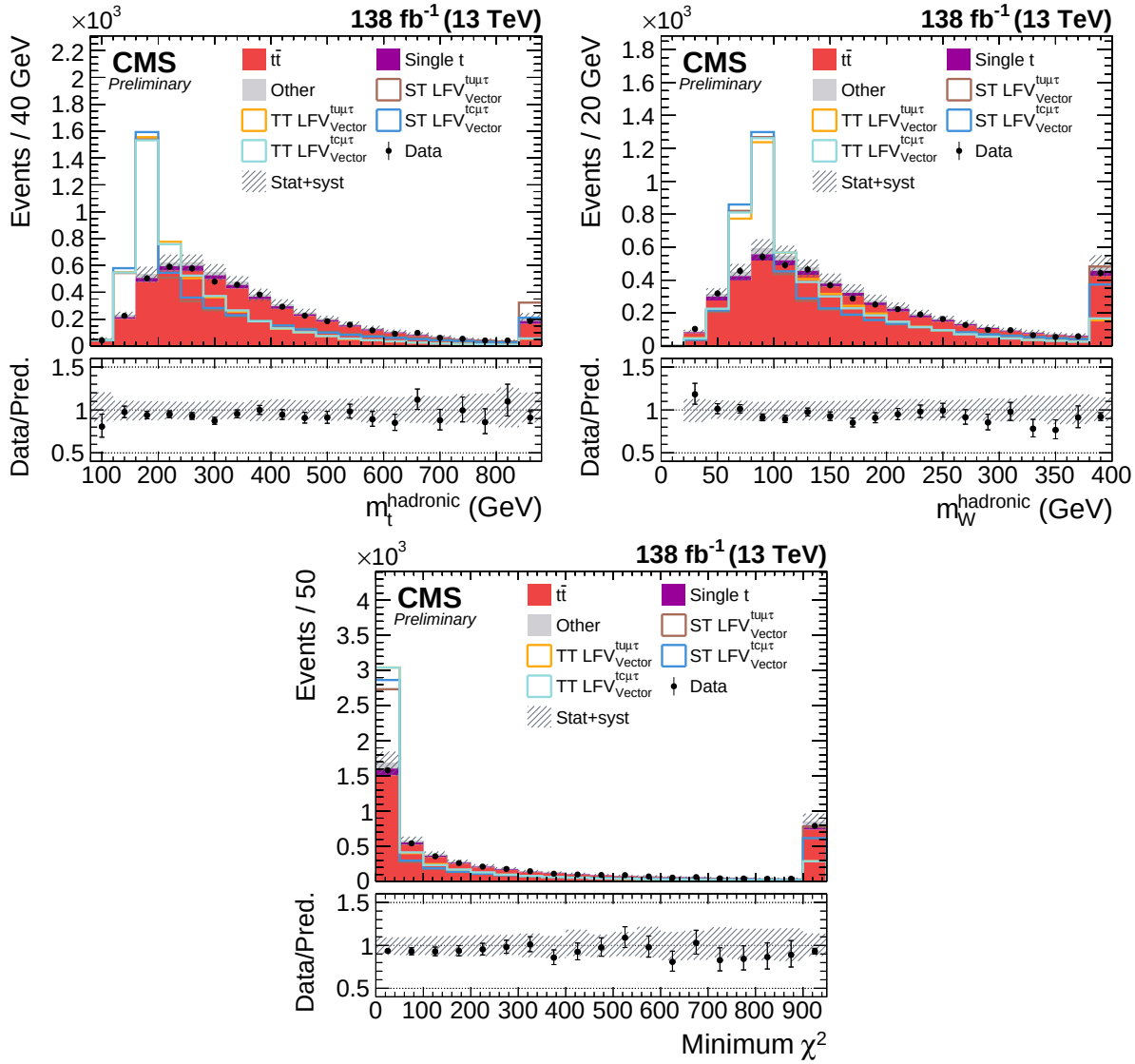

Figure 3: Distributions in the reconstructed top quark mass (top left), W boson mass (top right), and minimum χ^2 (bottom) from the top quark reconstruction. The solid lines show the signal distributions, individually for each type of operator and interaction. The signals are normalized to the total number of events in data for visibility. The last bin in each histogram contains the overflow. The shaded band displays the total uncertainty in the predicted background, consisting of statistical and systematic uncertainties. The panels below the distributions show the ratio of data to the background prediction.

Table 4: Input features of the DNN. The angular distance ΔR_{ij} between two objects i and j is defined as $\Delta R_{ij} = \sqrt{\Delta\eta_{ij}^2 + \Delta\phi_{ij}^2}$, where $\Delta\eta_{ij}$ and $\Delta\phi_{ij}$ are the differences in pseudorapidity and azimuthal angle, respectively.

Group	Variables	Description
Muon (μ)	$p_{\mathrm{T}\mu}$, η_μ	p_T and η of selected muon
Tau (τ_h)	$p_{\mathrm{T}\tau_\mathrm{h}}$, η_{τ_h}, m_{τ_h}	p_T, η, and mass of selected τ_h
Muon+Tau ($\mu\tau_\mathrm{h}$)	$m_{\mu\tau_\mathrm{h}}$, $\Delta\eta_{\mu\tau_\mathrm{h}}$, $\Delta\phi_{\mu\tau_\mathrm{h}}$, $\Delta R_{\mu\tau_\mathrm{h}}$	Mass and angular differences of $\mu\tau_\mathrm{h}$ system
Jets	$p_{\mathrm{T}1}$, $p_{\mathrm{T}2}$, $p_{\mathrm{T}3}$	p_T of jets ordered in increasing p_T
	η_1, η_2, η_3	η of jets ordered in increasing p_T
	m_1, m_2, m_3	Mass of jets ordered in increasing p_T
	b_1, b_2, b_3	b tagging discriminant of jets ordered in increasing p_T
Event	$p_\mathrm{T}^\mathrm{miss}$	Missing transverse momentum
t and W reco.	χ^2, $m_{\mathrm{bjj'}}$, $m_{\mathrm{jj'}}$	$minimum\chi^2$ and reconstructed t and W masses
	$\Delta\eta_{\mathrm{jj'}}$, $\Delta\phi_{\mathrm{jj'}}$, $\Delta R_{\mathrm{jj'}}$	Angular differences of jets used in W reco.

the reconstructed top quark and W boson masses, respectively, than the background distributions. The latter have broader distributions because of large contributions from dileptonic $\mathrm{t\bar{t}}$ events. Signal events show a noticeable peak at small values in the χ^2 distribution, more pronounced than the background. The data are described by the background simulation within the uncertainties.

6.2 Multivariate analysis using deep neural network

The discrimination between CLFV signals and background processes is performed using machine learning with a multiclass deep neural network (DNN) algorithm. The training of the DNN is performed using ST CLFV and TT CLFV signal samples and $\mathrm{t\bar{t}}$ background samples, because $\mathrm{t\bar{t}}$ constitutes the largest background in this analysis. The DNN model is trained to predict the probability p of an event belonging to one of the three classes ST CLFV, TT CLFV, and background. Events after the final selection are used for the training and the evaluation of the DNN. The three probabilities are combined into a single variable

$$\text{DNN score} = \frac{0.1p(\text{TT CLFV}) + 0.9p(\text{ST CLFV})}{p(\text{background})} \tag{4}$$

which we found to be an optimal choice for the best expected upper limits on the signal cross sections.

A single DNN classifier is trained for all data-taking periods, combining the different Lorentz structures and the two CLFV interactions $\mathrm{tu}\mu\tau$ and $\mathrm{tc}\mu\tau$. We balance the number of signal and background events in the training such that there is no statistical bias from a dominant class. About 150 000 simulated events are passed to the DNN for each of the background and the two signal classes, where 70% are used for the training and 30% for the validation of the DNN.

The input features of the DNN comprise 28 variables, which include kinematic features of individual physics objects and their combinations, and global event features such as $p_\mathrm{T}^\mathrm{miss}$ and variables from the χ^2 reconstruction. The input features together with a short description are

given in Table 4. The sensitivity of the DNN classifier is driven by the reconstructed top quark and W masses $m_{\mathrm{bjj'}}$ and $m_{\mathrm{jj'}}$, respectively, as well as the mass of the $\mu\tau_{\mathrm{h}}$ system $m_{\mu\tau_{\mathrm{h}}}$. Following these, the p_{T} of the muon and τ_{h} candidates contribute to the classifier performance.

We optimize the DNN design and hyperparameters in terms of its accuracy. The model is implemented in Keras [58] with the Tensorflow backend [59]. The Adam [60] optimization algorithm is used to minimize the sparse categorical cross-entropy loss function when updating the DNN parameters during the training. The DNN architecture consists of two hidden layers with 50 nodes, where the weights are initialised with randomly distributed weights following a normal distribution. We use the ReLu [61] activation function and a batch size of 1024 events in the training. The number of training iterations is automatically determined and the training is stopped if there is no improvement in the validation loss after 30 epochs.

7 Systematic uncertainties

Systematic uncertainties are considered for experimental sources and the modelling of simulated samples, including uncertainties in the predicted cross sections. The uncertainties generally change the normalization and the shape of the distributions in the DNN score. The different uncertainty sources are treated as nuisance parameters in a profile likelihood fit in the statistical evaluation of the results. The statistical uncertainty from the limited size of the simulated samples is treated following the Barlow-Beeston-light approach [62].

7.1 Experimental uncertainties

Integrated luminosity The uncertainties related to the luminosity measurement in each year change the normalization of the background prediction and are 1.2 [63], 2.3 [64], and 2.5% [65] for 2016, 2017, and 2018, respectively. The total uncertainty for all years combined is 1.6%, taking into account correlations in the luminosity measurement between the individual data-taking periods.

Pileup reweighting The uncertainty in the number of pileup interactions is estimated by varying the predicted inelastic cross section of 69.2 mb [66] by $\pm$4.6%. This source is considered to be correlated across all data-taking periods.

Trigger efficiency Data-to-simulation scale factors for the trigger efficiency are varied within their uncertainties for each data-taking period and are considered correlated between the periods. In addition, a gradual timing shift of the ECAL was not properly propagated to the L1 trigger inputs and caused an inefficiency by associating the input to the previous bunch crossing in 2016 and 2017, known as "prefiring" [14]. A similar effect is present in the muon system due to the limited time resolution of the subdetectors, mainly affecting the 2016 data, but also present in 2017 and 2018 where the effect is smaller. A corresponding correction is applied, and the uncertainties include a statistical component and a variation of this correction by $\pm$20%. This uncertainty is uncorrelated between data-taking periods.

Muon scale factors We apply corrections because of differences between data and simulation in the muon identification and isolation efficiencies. The corresponding uncertainties are derived during the determination of these scale factors in data samples enriched in $\mathrm{Z} \to \mu\mu$ events [17]. In addition to the uncertainties in the scale factors, an uncertainty for muons with p_{T} larger than 200 GeV is implemented, which increases linearly with increasing p_{T} [13]. The uncertainties related to the muon identification and isolation are correlated across the data-taking periods.

τ_h identification and energy scale Uncertainties in the identification efficiencies of the τ_h leptons against jets, muons, and electrons consist of several sources related to statistical and systematic components of the scale factor measurement. The uncertainties related to the τ_h discrimination against jets are further divided with respect to the data-taking period, the decay mode of the τ_h, and the p_T range [54]. The uncertainty in the τ_h energy scale is evaluated by shifting the τ_h momentum in simulated events within its uncertainty [53, 54]. The uncertainties in the τ_h identification against jets are partly correlated across the data-taking periods and the τ_h decay modes, depending on the source of uncertainty. Other uncertainties related to the τ_h identification and reconstruction are uncorrelated.

Background estimation for jets misidentified as τ_h The statistical uncertainty arising from the determination of the scaling factors for events with misidentified τ_h candidates is considered. In addition, a closure test is performed using simulated events for individual decay modes of the τ_h candidate and the different data-taking periods. The difference between the number of simulated background events and the number of events predicted by the ABCD method is considered as an uncertainty, and amounts to 2–3%. This uncertainty is uncorrelated for all data-taking periods.

Jet energy scale and resolution The uncertainties in the JES are estimated by shifting the jet momenta in simulated events within their uncertainties for several sources of the JES correction. The JER uncertainty is evaluated by changing the resolution in the simulation by one standard deviation [49]. An inefficiency caused by a non-functional HCAL module in 2018 results in an additional uncertainty, which is estimated by scaling down the jet energy in the affected detector region [67]. The JES and JER variations change the p_T and the energy of jets and are propagated to $\vec{p}_T^{\,miss}$. The JES uncertainties are correlated for some sources, while the uncertainties in JER are uncorrelated for all data-taking periods.

b tagging The scale factors and uncertainties related to the correction of the b tagging discriminant are evaluated separately for light-quark and gluon jets, and for b and c jets [50]. In addition, for each variation of the JES, dedicated scale factors are calculated and applied. The b tagging uncertainty sources include effects from the origin of jets and statistical uncertainties that arise from the scale factor measurement. The statistical components are uncorrelated between data-taking periods, while the others are fully correlated.

7.2 Modelling uncertainties

The modelling uncertainties are fully correlated through all data-taking periods unless stated otherwise.

PDF and the strong coupling Uncertainties in the PDF are estimated by reweighting events with the eigenvector variations of the NNPDF 3.1 set [39]. The PDF uncertainty is included for the $t\bar{t}$ background and signal samples. In addition, an uncertainty from the choice of the strong coupling α_S in the PDF set is taken into account [68] for the $t\bar{t}$ background simulation.

Missing higher orders The uncertainty from missing higher orders in the calculation of matrix elements (ME) for signal and $t\bar{t}$ background processes is estimated by varying the renormalization (μ_R) and factorization (μ_F) scales. We consider variations by factors of 2 and 0.5 in μ_R at a fixed value of μ_F, variations of μ_F for a fixed value of μ_R, and simultaneous variations of μ_R and μ_F. The resulting sources of uncertainty are further divided into four different regions

in muon and τ_h p_T, to address expected differences arising from additional jets in the TT CLFV signals at high lepton p_T.

Parton shower Uncertainties in the initial state (ISR) and final state radiation (FSR) are estimated by varying the scale of α_S in the parton shower (PS) by factors of 2 and 0.5 separately for the ISR and FSR. This uncertainty is included for signal and $t\bar{t}$ background samples.

Cross sections The uncertainties in the predicted cross sections are treated as several different normalization uncertainties. In $t\bar{t}$ production, scale variations and uncertainties in the PDF amount to a total uncertainty of 4.4% [22]. An uncertainty of 10% is assigned to single top quark production in the t channel, tW production, and to the other background processes.

ME-PS matching The damping of high p_T radiation in the matching of the ME and PS simulation is regulated by the parameter h_{damp} in POWHEG [69]. We estimate the uncertainty from the ME-PS matching by shifting $h_{damp} = 1.58^{+0.66}_{-0.59} m_t$ within its uncertainties, where m_t = 172.5 GeV. This uncertainty affects the $t\bar{t}$ background.

Underlying event The uncertainty related to the CP5 underlying event tune [40] of PYTHIA is evaluated from $t\bar{t}$ samples generated with modified tune parameters.

Top quark p_T reweighting The uncertainty arising from the modelling of the top quark p_T spectrum is evaluated by changes in the μ_R and μ_F scales in the NNLO calculation [27] for the determination of the reweighting correction.

8 Results

Distributions in the DNN score are investigated in search for CLFV interactions. We set upper limits at the 95% confidence level (CL) on the coupling modifier $\hat{\mu}$, which translates to limits on the Wilson coefficients $(C_a/\Lambda^2)^2$. To set these limits, we use a modified frequentist CL_s method [70, 71], which uses the profile likelihood ratio as the test statistic. The distributions in this test statistic are determined using an asymptotic approximation [72]. A binned maximum likelihood fit is constructed using the measured distribution in the DNN score, the simulated background processes, and the predicted CLFV signals. The systematic uncertainties described in Section 7 are included as nuisance parameters. The statistical analysis is performed using the CMS statistical analysis tool COMBINE [73], which is based on the ROOFIT [74] and ROOSTATS [75] frameworks. Upper limits on the individual coupling modifiers are calculated by performing a simultaneous fit to all data-taking periods.

Distributions in the DNN score are shown for two signal hypotheses in Fig. 4 after the binned maximum likelihood fit for all data-taking periods combined. At the highest value of the DNN score, corresponding to the histogram bin with the highest sensitivity to CLFV interactions, uncertainties of 15–20% in the background predictions are obtained, comparable to the statistical uncertainties in data. We observe no significant deviation from the SM predictions.

The one-dimensional upper limits on a specific Wilson coefficient are derived assuming positive values for $(C_a/\Lambda^2)^2$. The limits are calculated by taking the square root of the upper limits on the corresponding coupling modifier $\hat{\mu}_a$ for each CLFV interaction operator with $\Lambda = 1$ TeV. Upper limits on the branching fractions $\mathcal{B}(t \to \mu\tau q)$, with q = u or c, are calculated using Eq. (2) from Ref. [20]. Signal processes are considered separately for each Lorentz structure and quark flavour, assuming only one nonvanishing coupling at the same time. Limits on the

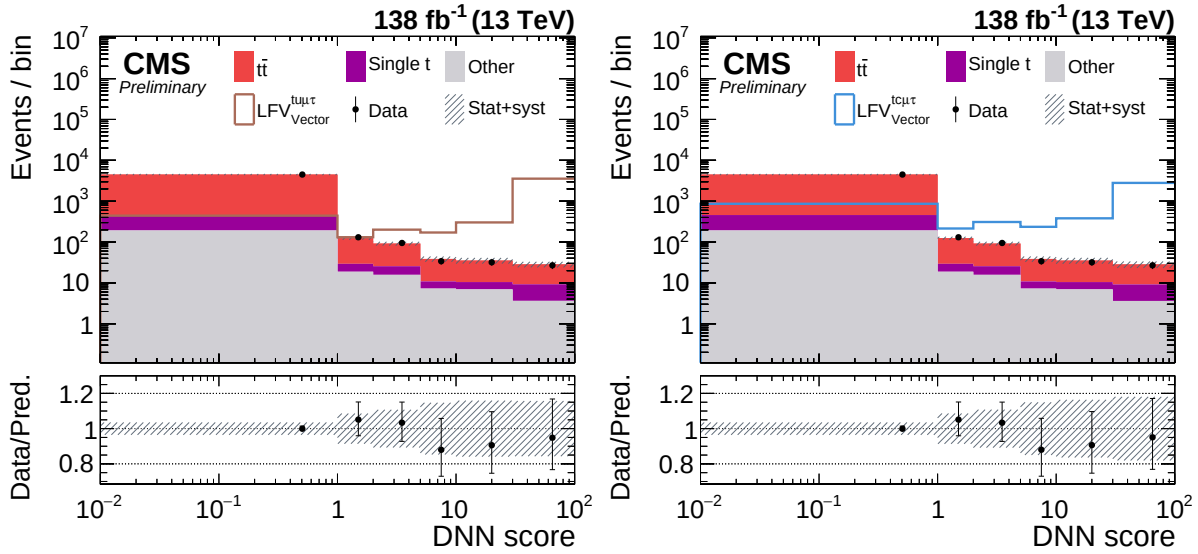

Figure 4: Combined distributions in the DNN score after the profile likelihood fit for all data-taking periods for the vector operators with tu$\mu\tau$ (left) and tc$\mu\tau$ (right) couplings. The signal distributions are normalized to the total number of events observed in the data. The last bin of each histogram contains the overflow. The hatched bands represent the total post-fit uncertainties in the background predictions, including statistical and systematic sources. The panels below the distributions show the ratio of data to the background prediction.

CLFV signal cross sections σ are calculated by multiplying the limit on the coupling modifier with the sum of the ST CLFV and TT CLFV cross sections from Table 2. In Table 5, the observed and expected upper limits on cross sections, Wilson coefficients, and branching fractions for each interaction are listed with the central probability intervals containing 68% of the expected upper limits.

We show exclusion contours calculated from the results of Table 5 in Fig. 5, obtained by assuming a linear relationship between the limits on $\mathcal{B}(\mathrm{t} \to \mu\tau\mathrm{c})$ and $\mathcal{B}(\mathrm{t} \to \mu\tau\mathrm{u})$ for each operator. The contours are shown in the plane of branching fractions (left) and Wilson coefficients (right) for the tu$\mu\tau$ and tc$\mu\tau$ couplings for scalar, vector, and tensor operators. In the ST CLFV processes, the cross sections corresponding to the tu$\mu\tau$ coupling are larger than those for the tc$\mu\tau$ coupling, resulting in more stringent constraints on the corresponding Wilson coefficients. The largest impact on the sensitivity of the results originates from the limited sample size in the last bin of the DNN score and the matrix element scale variations.

9 Conclusion

A search for charged-lepton flavour violation (CLFV) in the top quark sector has been presented. The search uses data corresponding to an integrated luminosity of 138 fb^{-1} collected by the CMS experiment during 2016–2018 in proton-proton (pp) collisions at a centre-of-mass energy of 13 TeV.

Interactions of a top quark with a muon, a tau lepton, and an up-type quark u or c are considered, where the scale of new physics responsible for CLFV is assumed to be larger than the energy scale of p p collisions at the LHC. The signal extraction is performed using measured distributions in a multiclass discriminator obtained with a deep neural network. No significant deviation is observed from the standard model background prediction and upper limits on the

Table 5: The 95% CL observed and expected upper limits on CLFV cross sections, Wilson coefficients $C_{tq\mu\tau}$, and branching fractions for different types of interactions and Lorentz structures. The expected upper limits are shown in brackets behind the observed limits. The central probability intervals containing 68% of the expected upper limits are given in square brackets below the upper limits.

Interaction	Type	σ [fb]	$C_{tq\mu\tau}/\Lambda^2$ [TeV^{-2}]	$\mathcal{B}(t \to \mu\tau q)[10^{-6}]$
$tu\mu\tau$	Scalar	2.039 (2.337) [1.574, 3.594]	0.182 (0.194) [0.16, 0.241]	0.040 (0.046) [0.031, 0.071]
	Vector	2.384 (2.746) [1.857, 4.213]	0.09 (0.096) [0.079, 0.119]	0.078 (0.09) [0.061, 0.138]
	Tensor	2.834 (3.326) [2.257, 5.063]	0.045 (0.049) [0.04, 0.06]	0.118 (0.138) [0.094, 0.211]
$tc\mu\tau$	Scalar	4.269 (5.02) [3.291, 8.142]	0.817 (0.886) [0.717, 1.128]	0.81 (0.953) [0.625, 1.545]
	Vector	7.213 (8.552) [5.663, 13.734]	0.419 (0.457) [0.372, 0.579]	1.71 (2.027) [1.342, 3.255]
	Tensor	7.927 (9.633) [6.427, 15.2]	0.188 (0.207) [0.169, 0.26]	2.052 (2.494) [1.664, 3.936]

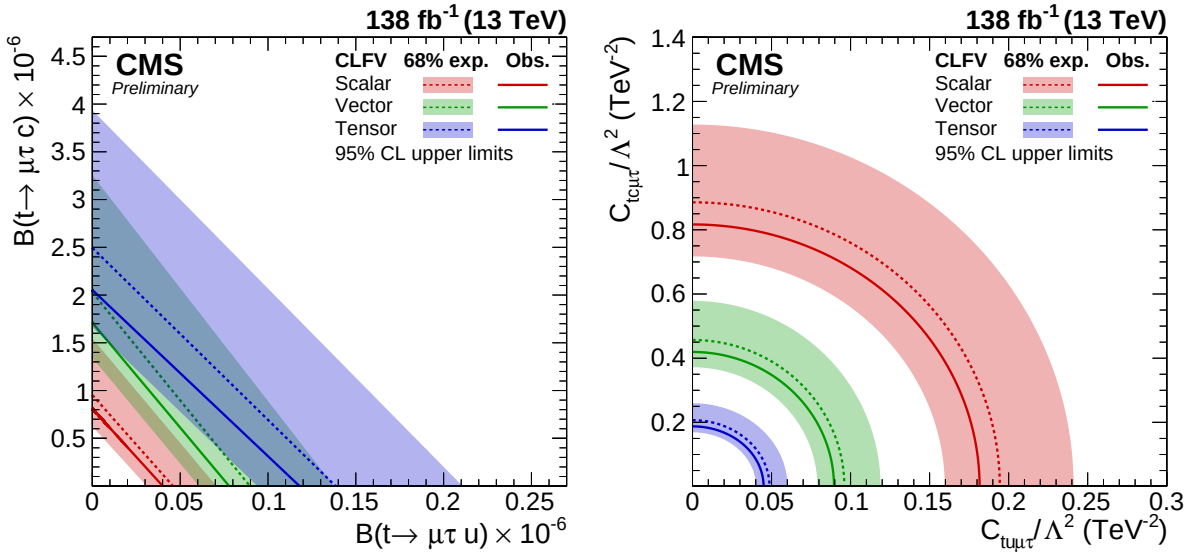

Figure 5: Exclusion contours for the observed and expected upper limits and central probability intervals containing 68% of the expected upper limits for the branching fractions (left) and Wilson coefficients (right) corresponding to the $tu\mu\tau$ and $tc\mu\tau$ couplings for scalar, vector and tensor Lorentz structures.

signal cross sections are set at 95% confidence level (CL). The limits are interpreted in terms of CLFV branching fractions ($\mathcal{B}$) of the top quark, resulting in $\mathcal{B}(\mathrm{t} \to \mu\tau\mathrm{u}) < 0.04$, 0.078, and 0.118×10^{-6}, and $\mathcal{B}(\mathrm{t} \to \mu\tau\mathrm{c}) < 0.81$, 1.71, and 2.05×10^{-6} at 95% CL for scalar, vector, and tensor-like operators, respectively. This search complements previous CMS results involving $\mathrm{e}\mu$ CLFV interactions [12, 13] and results in more stringent upper limits on Wilson coefficients in an effective field theory by approximately a factor of two compared to the latest experimental results involving $\mu\tau$ CLFV interactions [11].

References

[1] R. J. Gaitskell, "Direct detection of dark matter", *Ann. Rev. Nucl. Part. Sci.* **54** (2004) 315, doi:10.1146/annurev.nucl.54.070103.181244.

[2] V. Trimble, "Existence and nature of dark matter in the universe", *Ann. Rev. Astron. Astrophys.* **25** (1987) 425, doi:10.1146/annurev.aa.25.090187.002233.

[3] T. A. Porter, R. P. Johnson, and P. W. Graham, "Dark matter searches with astroparticle data", *Ann. Rev. Astron. Astrophys.* **49** (2011) 155, doi:10.1146/annurev-astro-081710-102528, arXiv:1104.2836.

[4] G. Bertone, D. Hooper, and J. Silk, "Particle dark matter: Evidence, candidates and constraints", *Phys. Rept.* **405** (2005) 279, doi:10.1016/j.physrep.2004.08.031, arXiv:hep-ph/0404175.

[5] A. D. Sakharov, "Violation of CP Invariance, C asymmetry, and baryon asymmetry of the universe", *Pisma Zh. Eksp. Teor. Fiz.* **5** (1967) 32, doi:10.1070/PU1991v034n05ABEH002497.

[6] R. Davis, Jr., D. S. Harmer, and K. C. Hoffman, "Search for neutrinos from the sun", *Phys. Rev. Lett.* **20** (1968) 1205, doi:10.1103/PhysRevLett.20.1205.

[7] L. Calibbi and G. Signorelli, "Charged lepton flavour violation: An experimental and theoretical introduction", *Riv. Nuovo Cim.* **41** (2018) 71, doi:10.1393/ncr/i2018-10144-0, arXiv:1709.00294.

[8] HFLAV Collaboration, "Averages of b-hadron, c-hadron, and τ-lepton properties as of 2021", *Phys. Rev. D* **107** (2023) 052008, doi:10.1103/PhysRevD.107.052008, arXiv:2206.07501.

[9] T. J. Kim et al., "Correlation between $R_{D^{(*)}}$ and top quark FCNC decays in leptoquark models", *JHEP* **07** (2019) 025, doi:10.1007/JHEP07(2019)025, arXiv:1812.08484.

[10] LHCb Collaboration, "Measurement of the ratios of branching fractions $\mathcal{R}(D^*)$ and $\mathcal{R}(D^0)$", *Phys. Rev. Lett.* **131** (2023) 111802, doi:10.1103/PhysRevLett.131.111802, arXiv:2302.02886.

[11] ATLAS Collaboration, "Search for charged-lepton-flavour violating $\mu\tau$qt interactions in top-quark production and decay in pp collisions at $\sqrt{s} = 13$ TeV with the ATLAS detector at the LHC", 2024. arXiv:2403.06742.

[12] CMS Collaboration, "Search for charged-lepton flavor violation in top quark production and decay in pp collisions at $\sqrt{s}$ = 13 TeV", *JHEP* **06** (2022) 082, doi:10.1007/JHEP06(2022)082, arXiv:2201.07859.

[13] CMS Collaboration, "Search for charged-lepton flavor violation in the production and decay of top quarks using trilepton final states in proton-proton collisions at $\sqrt{s} = 13$ TeV", 2023. arXiv:2312.03199.

[14] CMS Collaboration, "Performance of the CMS Level-1 trigger in proton-proton collisions at $\sqrt{s} = 13$ TeV", *JINST* **15** (2020) P10017, doi:10.1088/1748-0221/15/10/P10017, arXiv:2006.10165.

[15] CMS Collaboration, "The CMS trigger system", *JINST* **12** (2017) P01020, doi:10.1088/1748-0221/12/01/P01020, arXiv:1609.02366.

[16] CMS Collaboration, "The CMS experiment at the CERN LHC", *JINST* **3** (2008) S08004, doi:10.1088/1748-0221/3/08/S08004.

[17] CMS Collaboration, "Performance of the CMS muon detector and muon reconstruction with proton–proton collisions at $\sqrt{s} = 13$ TeV", *JINST* **13** (2018) P06015, doi:10.1088/1748-0221/13/06/P06015, arXiv:1804.04528.

[18] J. Alwall et al., "The automated computation of tree-level and next-to-leading order differential cross sections, and their matching to parton shower simulations", *JHEP* **07** (2014) 079, doi:10.1007/JHEP07(2014)079, arXiv:1405.0301.

[19] A. Dedes et al., "SmeftFR—Feynman rules generator for the Standard Model Effective Field Theory", *Comput. Phys. Commun.* **247** (2020) 106931, doi:10.1016/j.cpc.2019.106931, arXiv:1904.03204.

[20] J. Kile and A. Soni, "Model-independent constraints on lepton-flavor-violating decays of the top quark", *Phys. Rev. D* **78** (2008) 094008, doi:10.1103/PhysRevD.78.094008, arXiv:0807.4199.

[21] J. A. Aguilar-Saavedra, "Effective four-fermion operators in top physics: A roadmap", *Nucl. Phys. B* **843** (2011) 638, doi:10.1016/j.nuclphysb.2011.06.003, arXiv:1008.3562. [Erratum: doi:10.1016/j.nuclphysb.2011.06.003].

[22] M. Czakon and A. Mitov, "Top++: A program for the calculation of the top-pair cross-section at hadron colliders", *Comput. Phys. Commun.* **185** (2014) 2930, doi:10.1016/j.cpc.2014.06.021, arXiv:1112.5675.

[23] I. Brivio, "SMEFTsim 3.0 — a practical guide", *JHEP* **04** (2021) 073, doi:10.1007/JHEP04(2021)073, arXiv:2012.11343.

[24] CMS Collaboration, "Measurements of $\mathrm{t\bar{t}}$ differential cross sections in proton-proton collisions at $\sqrt{s} = 13$ TeV using events containing two leptons", *JHEP* **02** (2019) 149, doi:10.1007/JHEP02(2019)149, arXiv:1811.06625.

[25] CMS Collaboration, "Measurement of normalized differential $\mathrm{t\bar{t}}$ cross sections in the dilepton channel from pp collisions at $\sqrt{s} = 13$ TeV", *JHEP* **04** (2018) 060, doi:10.1007/JHEP04(2018)060, arXiv:1708.07638.

[26] CMS Collaboration, "Measurement of differential cross sections for top quark pair production using the lepton+jets final state in proton-proton collisions at 13 TeV", *Phys. Rev. D* **95** (2017) 092001, doi:10.1103/PhysRevD.95.092001, arXiv:1610.04191.

[27] M. Czakon et al., "Top-pair production at the LHC through NNLO QCD and NLO EW", *JHEP* **10** (2017) 186, doi:10.1007/JHEP10(2017)186, arXiv:1705.04105.

[28] CMS Collaboration, "Measurement of differential $\mathrm{t\bar{t}}$ production cross sections in the full kinematic range using lepton+jets events from proton-proton collisions at $\sqrt{s} = 13\,\text{TeV}$", *Phys. Rev. D* **104** (2021) 092013, doi:10.1103/PhysRevD.104.092013, arXiv:2108.02803.

[29] P. Nason, "A new method for combining NLO QCD with shower Monte Carlo algorithms", *JHEP* **11** (2004) 040, doi:10.1088/1126-6708/2004/11/040, arXiv:hep-ph/0409146.

[30] S. Frixione, P. Nason, and C. Oleari, "Matching NLO QCD computations with parton shower simulations: The POWHEG method", *JHEP* **11** (2007) 070, doi:10.1088/1126-6708/2007/11/070, arXiv:0709.2092.

[31] S. Alioli, P. Nason, C. Oleari, and E. Re, "A general framework for implementing NLO calculations in shower Monte Carlo programs: The POWHEG BOX", *JHEP* **06** (2010) 043, doi:10.1007/JHEP06(2010)043, arXiv:1002.2581.

[32] E. Re, "Single-top Wt-channel production matched with parton showers using the POWHEG method", *Eur. Phys. J. C* **71** (2011) 1547, doi:10.1140/epjc/s10052-011-1547-z, arXiv:1009.2450.

[33] M. Aliev et al., "HATHOR: HAdronic Top and Heavy quarks crOss section calculatoR", *Comput. Phys. Commun.* **182** (2011) 1034, doi:10.1016/j.cpc.2010.12.040, arXiv:1007.1327.

[34] P. Kant et al., "HATHOR for single top-quark production: Updated predictions and uncertainty estimates for single top-quark production in hadronic collisions", *Comput. Phys. Commun.* **191** (2015) 74, doi:10.1016/j.cpc.2015.02.001, arXiv:1406.4403.

[35] N. Kidonakis, "Two-loop soft anomalous dimensions for single top quark associated production with a W^- or H^-", *Phys. Rev. D* **82** (2010) 054018, doi:10.1103/PhysRevD.82.054018, arXiv:1005.4451.

[36] N. Kidonakis, "NNLL threshold resummation for top-pair and single-top production", *Phys. Part. Nucl.* **45** (2014) 714, doi:10.1134/S1063779614040091, arXiv:1210.7813.

[37] J. Alwall et al., "Comparative study of various algorithms for the merging of parton showers and matrix elements in hadronic collisions", *Eur. Phys. J. C* **53** (2008) 473, doi:10.1140/epjc/s10052-007-0490-5, arXiv:0706.2569.

[38] T. Sjöstrand et al., "An introduction to PYTHIA 8.2", *Comput. Phys. Commun.* **191** (2015) 159, doi:10.1016/j.cpc.2015.01.024, arXiv:1410.3012.

[39] NNPDF Collaboration, "Parton distributions from high-precision collider data", *Eur. Phys. J. C* **77** (2017) 663, doi:10.1140/epjc/s10052-017-5199-5, arXiv:1706.00428.

[40] CMS Collaboration, "Extraction and validation of a new set of CMS PYTHIA8 tunes from underlying-event measurements", *Eur. Phys. J. C* **80** (2020) 4, doi:10.1140/epjc/s10052-019-7499-4, arXiv:1903.12179.

[41] GEANT4 Collaboration, "GEANT4—a simulation toolkit", *Nucl. Instrum. Meth. A* **506** (2003) 250, doi:10.1016/S0168-9002(03)01368-8.

[42] CMS Collaboration, "Particle-flow reconstruction and global event description with the CMS detector", *JINST* **12** (2017) P10003, doi:10.1088/1748-0221/12/10/P10003, arXiv:1706.04965.

[43] CMS Collaboration, "Technical proposal for the Phase-II upgrade of the Compact Muon Solenoid", CMS Technical Proposal CERN-LHCC-2015-010, CMS-TDR-15-02, 2015.

[44] CMS Collaboration, "Muon identification using multivariate techniques in the CMS experiment in proton-proton collisions at $\sqrt{s} = 13$ TeV", *JINST* **19** (2024) P02031, doi:10.1088/1748-0221/19/02/P02031, arXiv:2310.03844.

[45] CMS Collaboration, "Electron and photon reconstruction and identification with the CMS experiment at the CERN LHC", *JINST* **16** (2021) P05014, doi:10.1088/1748-0221/16/05/P05014, arXiv:2012.06888.

[46] M. Cacciari, G. P. Salam, and G. Soyez, "The anti-k_{T} jet clustering algorithm", *JHEP* **04** (2008) 063, doi:10.1088/1126-6708/2008/04/063, arXiv:0802.1189.

[47] M. Cacciari, G. P. Salam, and G. Soyez, "FastJet user manual", *Eur. Phys. J. C* **72** (2012) 1896, doi:10.1140/epjc/s10052-012-1896-2, arXiv:1111.6097.

[48] M. Cacciari and G. P. Salam, "Dispelling the N^3 myth for the k_{T} jet-finder", *Phys. Lett. B* **641** (2006) 57, doi:10.1016/j.physletb.2006.08.037, arXiv:hep-ph/0512210.

[49] CMS Collaboration, "Jet energy scale and resolution in the CMS experiment in pp collisions at 8 TeV", *JINST* **12** (2017) P02014, doi:10.1088/1748-0221/12/02/P02014, arXiv:1607.03663.

[50] CMS Collaboration, "Identification of heavy-flavour jets with the CMS detector in pp collisions at 13 TeV", *JINST* **13** (2018) P05011, doi:10.1088/1748-0221/13/05/P05011, arXiv:1712.07158.

[51] E. Bols et al., "Jet flavour classification using DeepJet", *JINST* **15** (2020) P12012, doi:10.1088/1748-0221/15/12/P12012, arXiv:2008.10519.

[52] CMS Collaboration, "Performance of the DeepJet b tagging algorithm using 41.9/fb of data from proton-proton collisions at 13 TeV with Phase 1 CMS detector", CMS Detector Performance Summary CMS-DP-2018-058, 2018.

[53] CMS Collaboration, "Performance of reconstruction and identification of τ leptons decaying to hadrons and ν_τ in pp collisions at $\sqrt{s} = 13$ TeV", *JINST* **13** (2018) P10005, doi:10.1088/1748-0221/13/10/P10005, arXiv:1809.02816.

[54] CMS Collaboration, "Identification of hadronic tau lepton decays using a deep neural network", *JINST* **17** (2022) P07023, doi:10.1088/1748-0221/17/07/P07023, arXiv:2201.08458.

[55] CMS Collaboration, "Performance of missing transverse momentum reconstruction in proton-proton collisions at $\sqrt{s} = 13$ TeV using the CMS detector", *JINST* **14** (2019) P07004, doi:10.1088/1748-0221/14/07/P07004, arXiv:1903.06078.

[56] CMS Collaboration, "Measurement of the inclusive W and Z production cross sections in pp collisions at $\sqrt{s} = 7$ TeV", *JHEP* **10** (2011) 132, doi:10.1007/JHEP10(2011)132, arXiv:1107.4789.

[57] CDF Collaboration, "A measurement of $\sigma B(\mathrm{W} \to \mathrm{e}\nu)$ and $\sigma B(\mathrm{Z}^0 \to \mathrm{e}^+\mathrm{e}^-)$ in $\overline{\mathrm{p}}\mathrm{p}$ collisions at $\sqrt{s} = 1800$ GeV", *Phys. Rev. D* **44** (1991) 29, doi:10.1103/PhysRevD.44.29.

[58] F. Chollet et al., "Keras", 2017. https://keras.io.

[59] M. Abadi et al., "TensorFlow: Large-scale machine learning on heterogeneous systems", 2015. Software available from tensorflow.org. https://www.tensorflow.org/.

[60] D. P. Kingma and J. Ba, "Adam: A method for stochastic optimization", in *International Conference on Learning Representations (ICLR)*. San Diega, CA, USA, 2014. arXiv:1412.6980.

[61] A. F. Agarap, "Deep learning using rectified linear units (ReLU)", 2018. arXiv:1803.08375.

[62] J. S. Conway, "Incorporating nuisance parameters in likelihoods for multisource spectra", in *Proceedings, PHYSTAT 2011 Workshop on Statistical Issues Related to Discovery Claims in Search Experiments and Unfolding, CERN, Geneva, Switzerland, January 17-20, 2011*. 2011. arXiv:1103.0354. doi:10.5170/CERN-2011-006.115.

[63] CMS Collaboration, "Precision luminosity measurement in proton-proton collisions at $\sqrt{s} = 13$ TeV in 2015 and 2016 at CMS", *Eur. Phys. J. C* **81** (2021) 800, doi:10.1140/epjc/s10052-021-09538-2, arXiv:2104.01927.

[64] CMS Collaboration, "CMS luminosity measurement for the 2017 data-taking period at $\sqrt{s} = 13$ TeV", CMS Physics Analysis Summary CMS-PAS-LUM-17-004, 2018.

[65] CMS Collaboration, "CMS luminosity measurement for the 2018 data-taking period at $\sqrt{s} = 13$ TeV", CMS Physics Analysis Summary CMS-PAS-LUM-18-002, 2019.

[66] CMS Collaboration, "Measurement of the inelastic proton-proton cross section at $\sqrt{s} = 13$ TeV", *JHEP* **07** (2018) 161, doi:10.1007/JHEP07(2018)161, arXiv:1802.02613.

[67] CMS Collaboration, "Strategies and performance of the CMS silicon tracker alignment during LHC Run 2", *Nucl. Instrum. Meth. A* **1037** (2022) 166795, doi:10.1016/j.nima.2022.166795, arXiv:2111.08757.

[68] J. Butterworth et al., "PDF4LHC recommendations for LHC Run II", *J. Phys. G* **43** (2016) 023001, doi:10.1088/0954-3899/43/2/023001, arXiv:1510.03865.

[69] CMS Collaboration, "Investigations of the impact of the parton shower tuning in Pythia 8 in the modelling of $\mathrm{t\bar{t}}$ at $\sqrt{s} = 8$ and 13 TeV", CMS Physics Analysis Summary CMS-PAS-TOP-16-021, 2016.

[70] T. Junk, "Confidence level computation for combining searches with small statistics", *Nucl. Instrum. Meth. A* **434** (1999) 435, doi:10.1016/S0168-9002(99)00498-2, arXiv:hep-ex/9902006.

[71] A. Read, "Presentation of search results: The CL_s technique", *J. Phys. G* **28** (2002) 2693, doi:10.1088/0954-3899/28/10/313.

[72] G. Cowan, K. Cranmer, E. Gross, and O. Vitells, "Asymptotic formulae for likelihood-based tests of new physics", *Eur. Phys. J. C* **71** (2011) 1554, doi:10.1140/epjc/s10052-011-1554-0, arXiv:1007.1727. [Erratum: doi:10.1140/epjc/s10052-013-2501-z].

[73] CMS Collaboration, "The CMS statistical analysis and combination tool: COMBINE", 2024. arXiv:2404.06614. Submitted to *Comput. Softw. Big Sci.*

[74] W. Verkerke and D. P. Kirkby, "The RooFit toolkit for data modeling", in *Computing in High Energy and Nuclear Physics (CHEP03)*, L. Lyons and M. Karagoz, eds., volume C0303241, p. MOLT007. 2003. arXiv:physics/0306116.

[75] L. Moneta et al., "The RooStats project", in *Proceedings of the 13th International Workshop on Advanced Computing and Analysis Techniques in Physics Research*, T. Speer et al., eds., volume ACAT2010, p. 057. 2010. arXiv:1009.1003. doi:10.22323/1.093.0057.